applied optics

Fiber directional position sensor based on multimode interference imaging and machine learning

Kai Sun,[1,2,3] **Zhenming Ding,**[2,3] **and Ziyang Zhang**[2,3,*]

[1]*College of Optical Science and Engineering, Zhejiang University, Hangzhou 310027, Zhejiang Province, China*
[2]*Key Laboratory of 3D Micro/Nano Fabrication and Characterization of Zhejiang Province, School of Engineering, Westlake University, 18 Shilongshan Road, Hangzhou 310024, Zhejiang Province, China*
[3]*Institute of Advanced Technology, Westlake Institute for Advanced Study, 18 Shilongshan Road, Hangzhou 310024, Zhejiang Province, China*
Corresponding author: zhangziyang@westlake.edu.cn

A fiber directional position sensor based on multimode interference and image processing by machine learning is presented. Upon single-mode injection, light in multimode fiber generates a multi-ring-shaped interference pattern at the end facet, which is susceptible to the amplitude and direction of the fiber distortions. The fiber is mounted on an automatic translation stage, with repeating movement in four directions. The images are captured from an infrared camera and fed to a machine-learning program to train, validate, and test the fiber conditions. As a result, accuracy over 97% is achieved in recognizing fiber positions in these four directions, each with 10 classes, totaling an 8 mm span. The number of images taken for each class is merely 320. Detailed investigation reveals that the system can achieve over 60% accuracy in recognizing positions on a 5 μm resolution with a larger dataset, approaching the limit of the chosen translation stage.   © 2020 Optical Society of America

1. INTRODUCTION

Recent decades have witnessed tremendous development in the field of optical fiber sensors thanks to their extraordinary advantages such as the ability to sense and transmit signals in the same physical channel, immunity to electromagnetic interference, electrical insulation, and excellent stability in harsh and hazardous environments [1–3]. Fiber optical sensors have hence found wide applications in the structural health monitoring of buildings [4–6], earthquake detection [7], biosensing [8,9], tracking of robotic movement [10–12], etc. Recently, fiber vector sensors or shape sensors have attracted much attention as they provide not only the amplitude but also directional information about the signal. For shape sensing, the most frequently employed configurations are fiber grating structures [13–16] and inline fiber interferometers [17,18]. For the grating-based structures, the tracking of the bending direction is achieved by inscribing gratings in asymmetrical fibers such as eccentric core fibers [13], multi-core fibers [14], D-shaped cladding fibers [15], holey fibers [16], etc. The fabrication process is mostly complex and cost-sensitive. Inline fiber interferometers require accurate spectral detection and complicated analysis for signal interrogation due to the large number of densely packed peaks in the transmission spectrum.

On the other hand, machine learning becomes a powerful tool in solving many engineering problems. Multiple levels of abstraction are used to find the inner relationship among the complicated data by multilayer models [19–21]. Moreover, machine learning has succeeded in solving optical research problems such as microscopy resolution enhancement [22,23], optical experiment design [24], optical imaging [25–29], and optical communications [30]. Machine learning has greatly simplified the progress of information demodulation and analysis, and opens a door to research on complex images or patterns. In fiber sensors, specklegrams in the form of granular light-mode patterns generated from a multimode fiber have been studied by machine learning to decode the vectorial bend information or stresses applied in the fiber path [21,31,32]. However, due to the quasi-random nature of the specklegram, the analysis often takes much effort to interpret the relatively simple signals.

The current solutions for fiber vector sensors often require non-standard fiber forms and grating inscription [13–16], adding to the fabrication cost of the system. The spectroscopic methods involving interferometers and sharp filters demand accurate, stable, and often expensive spectral detection schemes to achieve high sensitivity [17,18]. Moreover, the work range is limited to the bandwidth of the system, and it is often difficult/costly to achieve fine spectral resolution over a broad

wavelength range. Fiber vector sensors using multimode interference (MMI) effect require only standard fibers for the light path. The intensity distribution of the 2D image at the fiber end-facet is captured by a standard camera to analyze the fiber deformation [33]. However, considering the large number of eigenmodes in the fiber, rigorous analysis of the image in relation to the actual fiber form becomes cumbersome using conventional numerical methods, such as eigenmode expansion and beam propagation methods, as each eigenmode has to be recalculated at every bending segment (upon weak arch approximation), causing simulation overload. An effective way to interrogate the obtained images is needed to further broaden the application of such MMI sensors.

Meanwhile, machine learning has become a powerful tool for image training and recognition. In this work, a directional position sensing system is first built based on the fiber MMI effect. A subsequent image recognition program is established by machine-learning algorithms to find the hidden correlation between the image pattern and fiber form without solving Maxwell's equations rigorously to pinpoint the exact solution. Care is taken to eliminate unwanted mechanical residue stresses along the fiber path so as to keep the interference images clean from random speckles. The images upon imposed bending by programmed positioning are collected automatically and fed to a convolutional neural network (CNN) model for data training.

In the following sections, optical theory, fiber sensor design, and experimental setups are explained in detail. The stability of the imaging system and repeatability of the fiber positioning system are also presented. In Section 4, the image collection processes are introduced, and the machine-learning method is applied to classify the images. Section 5 summarizes the results and shows that both directional and fine-resolution sensing ability can be achieved. Prospects for further development and applications are given in the Conclusion.

2. FIBER SENSOR DESIGN AND SIMULATIONS

Lumerical Mode Solution is an optical simulation software used to simulate the MMI structure consisting of the center-axis-aligned single-mode fiber (SMF) and multimode fiber (MMF). The SMF has a core diameter of 10.6 µm and a numerical aperture (NA) of 0.14. The MMF has a core diameter of 105 µm and a NA of 0.22. The cladding diameter of both fibers is 125 µm. In the simulation, the refractive index is set to 1.4567 for the SMF core and 1.4666 for the MMF core. The refractive index of the cladding is 1.45. The lengths of the SMF and MMF are 100 µm and 5 cm, respectively. Upon entering the MMF, the single-mode launch light at 1550 nm starts to overlap/couple with the eigenmodes in the MMF, and an intermodal interference develops along the fiber axis, as manifested by Fig. 1(a). To complete the simulation within reasonable time, only the first 500 eigenmodes are selected.

Since the structure is circularly symmetric with respect to the fiber axis, the interference pattern is accompanied by the self-imaging effects distributed in the radial plane in a concentric-ring pattern. The pattern at 20 mm, shown in Fig. 1(b), features a concentric ring structure with alternating light and dark zones. To verify the simulation, the MMF is first spliced to the SMF by a standard fusion splicer and then subsequently cleaved at a distance of 20 mm using a standard fiber cleaver (CT-50). A laser diode (LD) at 1550 nm is connected to the SMF. The output of the MMF is focused onto an infrared (IR) camera via a lens. The image, shown in Fig. 1(c), agrees well with the simulation.

Previous work has shown that the MMI image can reveal the vector bending information of the MMF but lacks a detailed interrogation program to recognize the fiber condition precisely [29]. In this work, an automatic directional positioning system is built to distort the MMF in controlled directions and steps. The collected images are fed to a machine-learning algorithm to train the dataset. In order to facilitate fiber mounting, the length of MMF in the experiment is taken as 85 mm. When the system
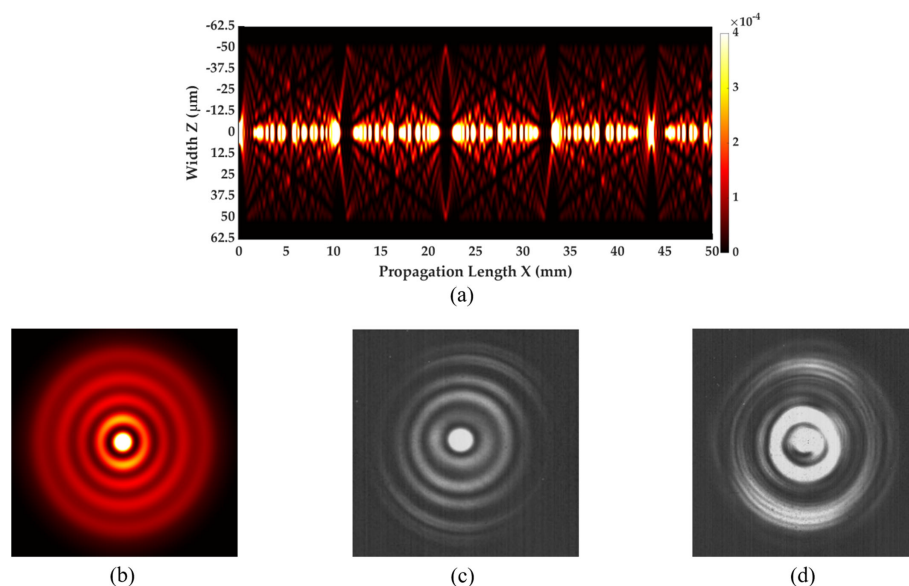

Fig. 1. (a) Intermodal interference profile inside the MMF along the fiber axis. (b) Simulated light intensity distribution, and (c) camera shot of the fiber MMI at 20 mm. (d) Camera shot of the fiber MMI at 85 mm.

is positioned at the initial "null" state, the undisturbed output image is shown in Fig. 1(d).

3. EXPERIMENT

A. Experimental Setup

The schematic of the experimental setup is described in Fig. 2(a), and the photo of the setup is shown in Fig. 2(b). The system adopts a handheld LD as light source. The input SMF is mounted on a budget three-dimension translation stage (E3030) by a homemade clamp. The clamp consists of a sub-holder with a sawed groove and a lid. The fiber can move freely in the groove but also follows smoothly the back-and-forth scanning movement of the stage. The movement range of the translation stage is 16 mm in the X, Y, and Z directions and the repeating accuracy is $\pm 2\ \mu m$. The minimal step, driven by a single electronic pulse, is $\sim 0.5\ \mu m$.

The open end of the MMF is securely fixed on a holder so that the imaging system stays in focus during the movement. The imaging system consists of a CCD camera (Xenics Bobcat-640-GigE, 640×512 pixel resolution, $20\ \mu m$ pixel pitch, and 100 Hz frame rate) and an objective lens (focal length 10 mm). A LabVIEW program was developed to control the movement pattern of the stage via a script and trigger the camera in a synchronized manner. All experiments are conducted at room temperature.

B. Stability and Repeatability

In order to evaluate the stability and repeatability of the system, the normalized average intensity variation (AIV) of the images is calculated upon different test settings. Normalized AIV, often used by researchers to find out the environmental impacts on the sensing system [34], is expressed as

$$\text{AIV} = \frac{1}{M \cdot X \cdot Y} \sum_{x=0}^{X-1} \sum_{y=0}^{Y-1} \left| S_{xy}^i - S_{xy}^1 \right|, \tag{1}$$

where S_{xy}^i represents the gray scale of pixels (from 0 to 65535, according to the light intensity received) at position (x, y) and
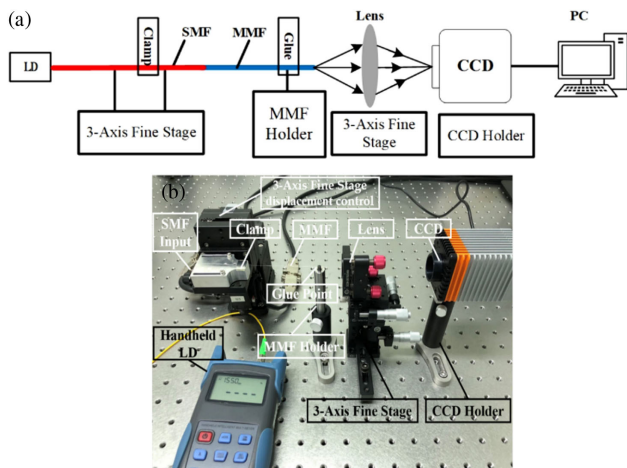

(a)

Fig. 2.   Schematic of experimental setup: (a) Schematic of the sensing system; (b) photo of the experimental setup.
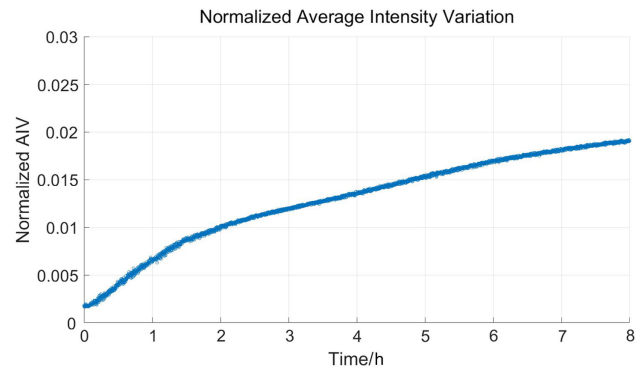

Fig. 3.   System stability study: AIV value increases slightly and tends to be stable over time.

S_{xy}^1 is the corresponding reference pixel at the initial condition. M equals 65535, the maximum gray scale of pixels.

To test the system stability, continuous camera shots were taken every 10 s for 8 h without moving the stage deliberately. The room was kept dark to eliminate the interference of natural light and fluorescent lamp. The first photo was calculated as the initial reference; AIV was then calculated and displayed in Fig. 3. The value increases slightly and tends to be stable. It could be caused by the temperature of the CCD camera after a long time working, as well as the instability of the handheld laser. In general, the AIV value stays and fluctuates within about 2%, which is considered low enough to conduct meaningful experiments.

The repeatability test of the fiber positioning system was performed as follows. The MMF was driven by the translation stage and moved back and forth between two positions, 0 mm and 5 mm, along the Y axis. As soon as the fiber arrives at these two positions, the CCD camera records an image. In total, 180 photos were taken for each position. The AIV values were calculated as shown in Fig. 4(a). The blue line with circles shows the AIV at 0 mm and the red line with asterisks shows the AIVs at 5 mm. The reference images in the AIV calculations are taken as the first photo at their respective positions. Though the values fluctuate, all remain below the 2% mark.

Figure 4(b) shows the other test. It describes the changes of AIV when fiber is moved from 0 to 5 mm and back by a step of 10 μm. The MMI images at each position were recorded, and corresponding AIVs were calculated with the same reference condition at 0 mm. AIVs changed smoothly and can almost coincide with each other for the forward and backward movements. It can be seen that during the reciprocating motion of the fiber, the AIV values stay almost the same when the fiber arrives at the same position, regardless of the forward or backward movement. This good repeatability is achieved by designing a suitable clamp that allows the free movement of the fiber but also enforces a responsive movement following the stage.

4. PROCESSING METHOD

A. Data Collection

The machine-learning process can take a considerable amount of time, and the experiments are designed in an efficient way to demonstrate the concept. The system is scripted to move and
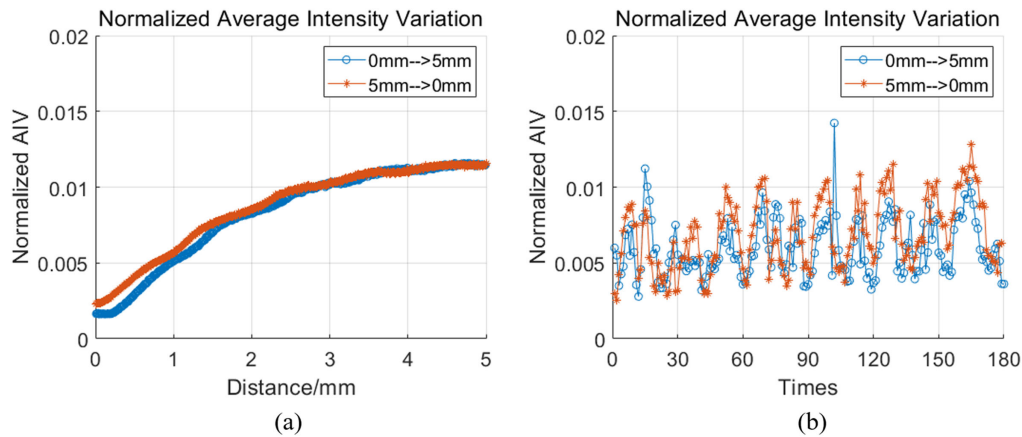
Fig. 4.   Results of the system repeatability study using AIV: (a) AIV values at 0 mm (blue circles) and 5 mm (red asterisks); (b) AIV values when the stage moves from 0 to 5 mm and back.
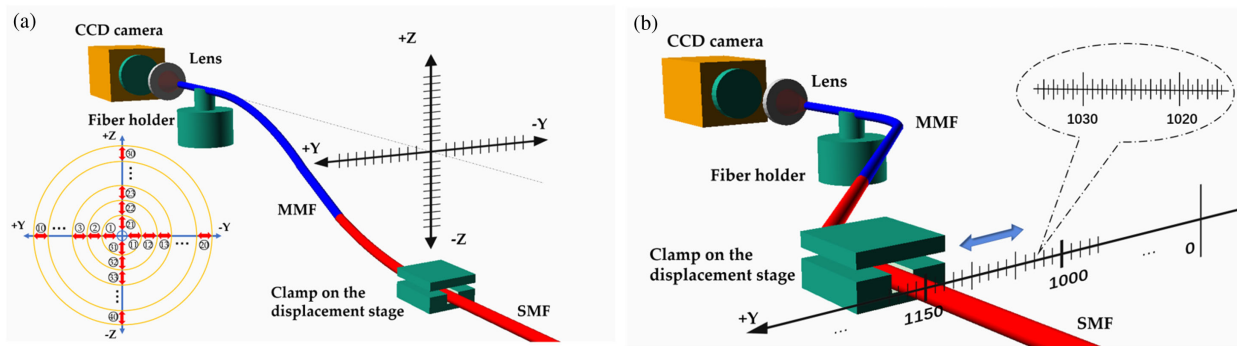

Fig. 5.   (a) Stage movement pattern for directional sensing. 10 classes of positions are formed along each of the four axes ($+Y$, $-Y$, $+Z$, $-Z$), with a span of 8 mm. (b) Stage movement pattern for the investigation of the fine spatial resolution within a small range along $+Y$.

collect images automatically for 1) pattern recognition from different positions with relatively large distances along 4 axes ($+Y$, $-Y$, $+Z$ and $-Z$) to test the directional sensing ability and 2) positioning studies from a fixed distance but with small steps along a given direction ($+Y$) to test the spatial resolution of the sensing system.

Figure 5(a) illustrates the directional sensing experiment. The fiber was driven to move along the negative and positive Y and Z axes. Each of the four axes is divided into 10 regions/classes with equal distance of 0.8 mm. The movement step is set to 2.5 μm so that each class contains 320 positions. Each position corresponds to a certain fiber form, consisting of a series of bends in the 3D space. The system is first initialized at the 0 μm position with a good multi-ring interference pattern as shown in Fig. 1(d). The stage is then scripted to move and drive the fiber in the following pattern $0 \rightarrow +Y \rightarrow 0 \rightarrow -Y \rightarrow 0 \rightarrow +Z \rightarrow 0 \rightarrow -Y \rightarrow 0$. Upon arriving at each position, the stage waits 2 s, leaving enough time for the mechanical system to stabilize, as well as for the camera to take and save the image.

Figure 5(b) illustrates the experiment for the positioning resolution study. The step was set to the minimal values of 0.5 μm as allowed by the control system, and a scanning movement was carried out repeatedly between the two positions at $Y = 1000$ μm and $Y = 1150$ μm for 360 rounds. The camera

takes a photo after each 0.5 μm movement completes, and in total 108,000 photos are collected and used to classify the 300 positions.

Polarization control is neglected in this experiment, as the effect of different polarization modes in the MMF upon deformation is lumped into the MMI image for subsequent data training. However, the long-time drifting of the polarization states, e.g., through temperature gradient, mechanical vibrations, or other changes in the working environment, can reduce the effectiveness of the short-time trained model without considering the polarization effect.

B. Machine Learning

In the experiments, a great number of photos in the format of binary files from the LabVIEW program were collected. For the machine-learning algorithm, they were first classified and processed. Then, the labeled photos were trained, validated, and tested by 18-layer residual networks (ResNet) [35]. The whole progress was carried out in the environment of Python-3.7.3 and Pytorch-1.3.1, running on Windows 10.

Among the many commonly used CNNs, 18-layer ResNet is chosen because it has relatively higher accuracy and fewer computational operations [36]. The ResNet codes from GitHub of Pytorch [37] were used in this paper. The structure of the
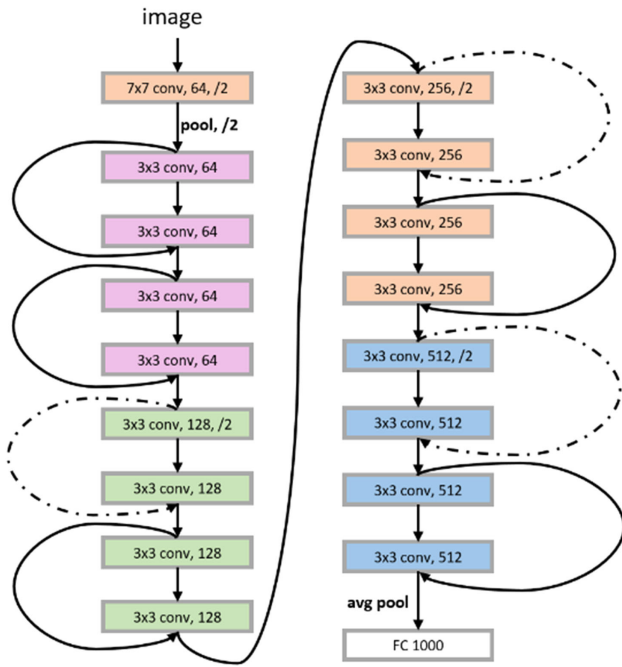
Fig. 6.   Structure of simplification for 18-layer ResNet.

Fig. 7.   Cross-entropy loss reduces during training steps. The inset table lists the final accuracy.

Table 1.   Train and Test Accuracy on Level of 5–75 μm Interval[a]

Interval/μm	Classes	Photos	Train Accuracy	Test Accuracy
5	6	300	17.22%	16.39%
15	6	300	30.22%	33.33%
25	6	300	71.94%	71.39%
50	3	300	70.40%	65.56%
75	2	300	95.00%	96.67%

[a]Each class contains 300 photos.

algorithm is shown in Fig. 6. The input image is firstly filtered to 64 channels by a 7×7 kernel filter and stride of 2. The rest blocks are convoluted by 3×3 kernel filters. The skip connection arrow shortcuts the two blocks to avoid gradient vanishing, which is the key competence of the ResNet algorithm. The following blocks, with three other colors, do similar computations except the dotted line with the arrow. Between blocks with different colors, a pooling layer is used and the output shape is reduced by half. In every single block, convolution, batch normalization, and ReLU layers are included. Eventually, after all convolutional operations, global average pooling, fully connected layer, and Softmax are used to calculate probabilities and give corresponding classifications.

5. RESULTS AND DISCUSSION

For the directional sensing experiment, there are 40 classes with equal distances on the four axes, consisting of over 12,800 photos. For machine learning, 60% of these photos are randomly chosen for training, 20% for validation, and the remaining 20% are used for testing. Figure 7 shows the cross-entropy loss of the model during training. It drops dramatically, then waves and approaches to zero. In the end, a training accuracy of 97.15% is reached and the test accuracy is 97.34%, as listed in the inset table.

The results have clearly demonstrated the sensitivity of multi-ring pattern to vectorial fiber deformation, as the bending/shape changes in different directions have strong rules and characteristics that can be extracted and summarized by machine-learning algorithms. Using 320 photos for one class is not a big dataset, but it still leads to a high accuracy of over 97%.

To give a rough impression of the spatial resolutions this system can achieve, the following tests are performed, as shown in Table 1, using 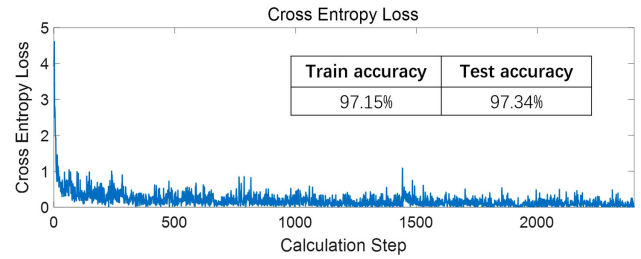the 108,000 photos from the experiment shown in Fig. 5(b). Only 300 photos from different positions are randomly selected for one class. Due to the quantity limit of datasets, some categories of intervals can only be divided into fewer classes. Generally, the train and test accuracies increase with greater intervals. When the photos are classified on the level of 75 μm, a result of accuracy 95% can be achieved, which means the sensing system can recognize well with this resolution level with only a small quantity of photos. When the interval is 25 μm, the sensing system can get higher accuracy of up to 70%. However, the system did not perform well on finer resolutions, and the accuracy of 5 μm interval is close to its random probability (16.67%). The results could be a result of the small quantity of the datasets as well as their diversity.

Investigation went on with finer resolutions for higher accuracy with bigger datasets. The interval between 5 and 50 μm is focused and the quantity of the datasets for each class is increased to 1000, as shown in Table 2. Overall accuracy is much improved for finer resolution. When the interval is greater than 10 μm, the accuracy goes beyond 80%. Even for an interval of 5 μm, the accuracy reaches 60%. As the translation stage is a budget model with a position-repeating accuracy of ± 2 μm,

Table 2.   Train and Test Accuracy on Level of 5–75 μm Interval[a]

Interval/μm	Classes	Photos	Train Accuracy	Test Accuracy
5	10	1000	60.15%	60.50%
7.5	10	1000	65.10%	66.15%
10	10	1000	80.20%	82.10%
15	10	1000	85.10%	86.30%
20	7	1000	86.57%	86.07%
50	3	1000	87.33%	88.50%
75	2	1000	99.83%	99.75%

[a]Each class contains 1000 photos.

Table 3.   Additional Test Accuracy of the 75 μm Case Using Models I–III[a]

Test Data Source	Round 1	Round 60	Round 120	Round 180	Round 240	Round 300	Round 360
Model I	50.33%	94.98%	49.83%	49.83%	49.83%	49.83%	49.83%
Model II	83.67%	50.17%	56.52%	92.64%	79.26%	98.66%	82.27%
Model III	81.99%	91.31%	97.66%	93.65%	74.58%	73.91%	83.61%

[a]Model I training data from round Nos. 50 and 51 only, Model II training data from round Nos. 1 and 360 only; Model III training dataset is formed by taking two photos from each round from Nos. 1 to 300.

the results have shown its potential in detecting fine position changes of a mechanical system.

The diversity and richness of data also play an important role in the training process. As mentioned in Section 4.A, 300 photos for each round and a total of 360 rounds were collected from the experiment. In Table 1, the model (Model I) takes the images only from Rounds 50 and 51 for training, validation, and test. Additionally, Model II is trained with images only from Rounds 1 and 360, while Model III takes two images from every round from numbers 1 to 300. For all three models, the remaining untrained data are used for test purposes and the results are summarized in Table 3. Close to the training data (Nos. 50 and 51), Model I works well, but the accuracy deteriorates quickly when the test data moves further to other rounds, down to complete randomness (∼50%). Model II works better for a broader selection of data rounds, but loses its accuracy between Nos. 60 and 120. Model III performs well in general, providing a good accuracy in almost all the data rounds. Comparing the three models, it can be seen that richness and diversity in data selection can greatly improve the model robustness.

It is worth noting that though high accuracy can be achieved in detecting fiber positions using the CNN method on large, rich, balanced datasets, the interrogation scheme is still of a probabilistic nature, i.e., errors may occur even in well-trained scenarios. For the traditional spectroscopic method using gratings and inline interferometers, detection can be theoretically unambiguous and practically only subject to system noise and errors.

The strength of using CNN in this work may be manifested in its generality and scalability. Traditional spectroscopic method suffers from a dilemma: it is difficult to achieve both fine resolution and large work range at reasonable cost. The CNN method can in principle train any images, even when the fiber is heavily distorted, and fine resolution can still be achieved so long as a sufficient number of images are collected for the training. The resolution of 5 μm and work range of ±8 mm demonstrated in this work is limited by the available budget motor-stage. Future work will be done to expand this limit.

Due to its probabilistic nature, the CNN method is not suitable for applications that are risky for catastrophic failure consequences, nor for systems that require high-level security. But thanks to its simple, scalable nature and the great flexibility of fibers, the proposed method may be a powerful auxiliary tool for tracking the directional movement of any mechanical parts.

6. CONCLUSION

In recent years, with the development of robots and unmanned automobiles, there has been huge demand for simple and practical fiber sensors. This paper proposes a novel fiber directional position sensor based on MMI and machine learning. With one simple fiber spliced by a standard SMF and MMF, directions and positions of displacement can be detected. Moreover, machine learning is used to analyze and distinguish the multi-ring patterns instead of the traditional interrogation system. In experiments, accuracy over 97% was achieved when the ResNet-18 algorithm was used to recognize multi-ring patterns from four different directions with an 800 μm spatial resolution, using a dataset of merely 320 photos for each class. Moreover, the system can achieve over 60% accuracy for a fine resolution of 5 μm when the dataset is enlarged to 1000 photos.

For future work, efforts will be made to enhance the spatial resolution by upgrading the translation stage and improving the fiber–clamp mechanics. Deeper neural networks and smarter selection of datasets are also expected to help reduce perturbations from environments on the multi-ring patterns. We believe this work will provide an alternative solution to building a low-cost directional position senor for mechanics and aerospace systems.

Disclosures.   The authors declare no conflicts of interest.

REFERENCES

1. A. D. Kersey, M. A. Davis, H. J. Patrick, M. LeBlanc, K. P. Koo, C. G. Askins, M. A. Putnam, and E. J. Friebele, "Fiber grating sensors," J. Lightwave Technol. **15**, 1442–1463 (1997).
2. B. H. Lee, Y. H. Kim, K. S. Park, J. B. Eom, M. J. Kim, B. S. Rho, and H. Y. Choi, "Interferometric fiber optic sensors," Sensors **12**, 2467–2486 (2012).
3. S. Cięszczyk and P. Kisała, "Inverse problem of determining periodic surface profile oscillation defects of steel materials with a fiber Bragg grating sensor," Appl. Opt. **55**, 1412–1420 (2016).
4. K. Bremer, F. Weigand, Y. Zheng, L. S. Alwis, R. Helbig, and B. Roth, "Structural health monitoring using textile reinforcement structures with integrated optical fiber sensors," Sensors **17**, 345 (2017).
5. T. H. Nguyen, T. Venugopala, S. Chen, T. Sun, K. T. Grattan, S. E. Taylor, P. A. M. Basheer, and A. E. Long, "Fluorescence based fibre optic pH sensor for the pH 10–13 range suitable for corrosion monitoring in concrete structures," Sens. Actuat. B **191**, 498–507 (2014).
6. C. H. Tan, Y. G. Shee, B. K. Yap, and F. M. Adikan, "Fiber Bragg grating based sensing system: early corrosion detection for structural health monitoring," Sens. Actuat. A **246**, 123–128 (2016).
7. A. H. Hartog, M. Belal, and M. A. Clare, "Advances in distributed fiber-optic sensing for monitoring marine infrastructure, measuring the deep ocean, and quantifying the risks posed by seafloor hazards," Mar. Technol. Soc. J. **52**, 58–73 (2018).

8. M. Loyez, J. Albert, C. Caucheteur, and R. Wattiez, "Cytokeratins biosensing using tilted fiber gratings," Biosensors **8**, 74 (2018).

9. M. Loyez, C. Ribaut, C. Caucheteur, and R. Wattiez, "Functionalized gold electroless-plated optical fiber gratings for reliable surface biosensing," Sens. Actuat. B **280**, 54–61 (2019).

10. S. Sareh, Y. Noh, M. Li, T. Ranzani, H. Liu, and K. Althoefer, "Macrobend optical sensing for pose measurement in soft robot arms," Smart Mater. Struct. **24**, 125024 (2015).

11. C. Zhu, X. Guan, X. Wang, Y. Li, E. Chalmers, and X. Liu, "Mussel—inspired flexible, durable, and conductive fibers manufacturing for finger—monitoring sensors," Adv. Mater. Interfaces **6**, 1801547 (2019).

12. M. Borot de Battisti, B. Denis de Senneville, M. Maenhout, J. J. Lagendijk, M. van Vulpen, G. Hautvast, D. Binnekamp, and M. A. Moerland, "Fiber Bragg gratings—based sensing for real—time needle tracking during MR—guided brachytherapy," Med. Phys. **43**, 5288–5297 (2016).

13. Y. Ou, J. Liu, X. Xu, Y. Zhao, and A. Zhou, "Phase-shifted eccentric core fiber Bragg grating fabricated by electric arc discharge for directional bending measurement," Sensors **18**, 1207 (2018).

14. I. Floris, S. Sales, P. A. Calderón, and J. M. Adam, "Measurement uncertainty of multicore optical fiber sensors used to sense curvature and bending direction," Measurement **132**, 35–46 (2019).

15. D. Zhao, X. Chen, K. Zhou, L. Zhang, I. Bennion, W. N. MacPherson, J. S. Barton, and D. C. Jones, "Bend sensors with direction recognition based on long period gratings written in D-shaped fiber," Appl. Opt. **43**, 5425–5428 (2004).

16. Y. G. Han, G. Kim, K. Lee, S. Lee, H. Chang, C. Oh, and J. Hee, "Bending sensitivity of long-period fiber gratings inscribed in holey fibers depending on an axial rotation angle," Opt. Express **15**, 12866–12871 (2007).

17. Y. Zhao, A. Zhou, H. Guo, Z. Zheng, Y. Xu, C. Zhou, and L. Yuan, "An integrated fiber Michelson interferometer based on twin-core and side-hole fibers for multi-parameter sensing," J. Lightwave Technol. **36**, 993–997 (2017).

18. H. Qu, G. F. Yan, and M. Skorobogatiy, "Interferometric fiber-optic bending/nano-displacement sensor using plastic dual-core fiber," Opt. Lett. **39**, 4835–4838 (2014).

19. J. Schmidhuber, "Deep learning in neural networks: an overview," Neural Netw. **61**, 85–117 (2015).

20. P. Fan, T. Zhao, and L. Su, "Deep learning the high variability and randomness inside multimode fibers," Opt. Express. **27**, 20241–20258 (2019).

21. A. R. Cuevas, M. Fontana, L. Rodriguez-Cobo, M. Lomer, and J. M. Lopez-Higuera, "Machine learning for turning optical fiber speck-legram sensor into a spatially-resolved sensing system. Proof of concept," J. Lightwave Technol. **36**, 3733–3738 (2018).

22. Y. Rivenson, Z. Gorocs, H. Gunaydin, Y. B. Zhang, H. D. Wang, and A. Ozcan, " Deep learning microscopy," Optica **4**, 1437–1443 (2017).

23. E. Nehme, L. E. Weiss, T. Michaeli, and Y. Shechtman, "Deep-STORM: super-resolution single-molecule microscopy by deep learning," Optica **5**, 458–464 (2018).

24. A. A. Melnikov, H. Poulsen Nautrup, M. Krenn, V. Dunjko, M. Tiersch, A. Zeilinger, and H. J. Briegel, "Active learning machine learns to create new quantum experiments," Proc. Natl. Acad. Sci. USA **115**, 1221–1226 (2018).

25. S. Li, M. Deng, J. Lee, A. Sinha, and G. Barbastathis, "Imaging through glass diffusers using densely connected convolutional networks," Optica **5**, 803–813 (2018).

26. B. Rahmani, D. Loterie, G. Konstantinou, D. Psaltis, and C. Moser, "Multimode optical fiber transmission with a deep learning network," Light Sci. Appl. **7**, 1–11 (2018).

27. N. Borhani, E. Kakkava, C. Moser, and D. Psaltis, "Learning to see through multimode fibers," Optica **5**, 960–966 (2018).

28. S. Aisawa, K. Noguchi, and T. Matsumoto, "Remote image classification through multimode optical fiber using a neural network," Opt. Lett. **16**, 645–647 (1991).

29. T. Matsumoto, M. Koga, K. Noguchi, and S. Aizawa, "Proposal for neural-network applications to fiber-optic transmission," in *IJCNN International Joint Conference on Neural Networks* (IEEE, 1990), 75–80.

30. S. Lohani, E. M. Knutson, M. O'Donnell, S. D. Huver, and R. T. Glasser, "On the use of deep neural networks in optical communications," Appl. Opt. **57**, 4180–4190 (2018).

31. W. B. Spillman, B. R. Kline, L. B. Maurice, and P. L. Fuhr, "Statistical mode sensor for fiber optic vibration sensing uses," Appl. Opt. **28**, 3166–3176 (1989).

32. O. Kotov, I. Chapalo, and A. Petrov, "Distributed interference multimode fiber sensor with disturbances localization ability," in *IEEE International Conference on Electrical Engineering and Photonics* (2018).

33. Z. Zhang, A. Rahman, J. Fiebrandt, Y. Wang, K. Sun, J. Luo, and M. M. Roth, "Fiber vector bend sensor based on multimode interference and image tapping," Sensors **19**, 321 (2019).

34. P. Wu, S. Zhu, M. Hong, F. Chen, and H. Liu, "Specklegram temperature sensor based on femtosecond laser inscribed depressed cladding waveguides in Nd: YAG crystal," Opt. Laser Technol. **113**, 11–14 (2019).

35. K. He, X. Zhang, S. Ren, and J. Sun, "Deep residual learning for image recognition," in *IEEE Conference on Computer Vision and Pattern Recognition (CVPR)* (2015).

36. C. Kawatsu, F. Koss, A. Gillies, A. Zhao, J. Crossman, B. Purman, D. Stone, and D. Dahn, "Gesture recognition for robotic control using deep learning," in *NDIA Ground Vehicle Systems Engineering and Technology Symposium* (2017).

37. https://github.com/pytorch/vision/blob/master/torchvision/models/resnet.py.